FRONTIERS OF PHYSICS

TOPICAL REVIEW
Volume 17 / Issue 6 / 63601 / 2022

Improving the device performances of two-dimensional semiconducting transition metal dichalcogenides: Three strategies

Mo Cheng[1,*], Junbo Yang[1,*], Xiaohui Li[1,*], Hui Li[1,*], Ruofan Du[1], Jianping Shi[1,†], Jun He[2,‡]

1 The Institute for Advanced Studies, Wuhan University, Wuhan 430072, China
2 Key Laboratory of Artificial Micro- and Nano-structures of Ministry of Education, School of Physics and Technology, Wuhan University, Wuhan 430072, China
Corresponding authors. E-mail: †jianpingshi@whu.edu.cn, ‡He-jun@whu.edu.cn
*These authors contributed equally to this work.
Received May 21, 2022; accepted June 23, 2022

ABSTRACT

Two-dimensional (2D) semiconductors are emerging as promising candidates for the next-generation nanoelectronics. As a type of unique channel materials, 2D semiconducting transition metal dichalcogenides (TMDCs), such as MoS_2 and WS_2, exhibit great potential for the state-of-the-art field-effect transistors owing to their atomically thin thicknesses, dangling-band free surfaces, and abundant band structures. Even so, the device performances of 2D semiconducting TMDCs are still failing to reach the theoretical values so far, which is attributed to the intrinsic defects, excessive doping, and daunting contacts between electrodes and channels. In this article, we review the up-to-date three strategies for improving the device performances of 2D semiconducting TMDCs: (i) the controllable synthesis of wafer-scale 2D semiconducting TMDCs single crystals to reduce the evolution of grain boundaries, (ii) the ingenious doping of 2D semiconducting TMDCs to modulate the band structures and suppress the impurity scatterings, and (iii) the optimization design of interfacial contacts between electrodes and channels to reduce the Schottky barrier heights and contact resistances. In the end, the challenges regarding the improvement of device performances of 2D semiconducting TMDCs are highlighted, and the further research directions are also proposed. We believe that this review is comprehensive and insightful for downscaling the electronic devices and extending the Moore's law.

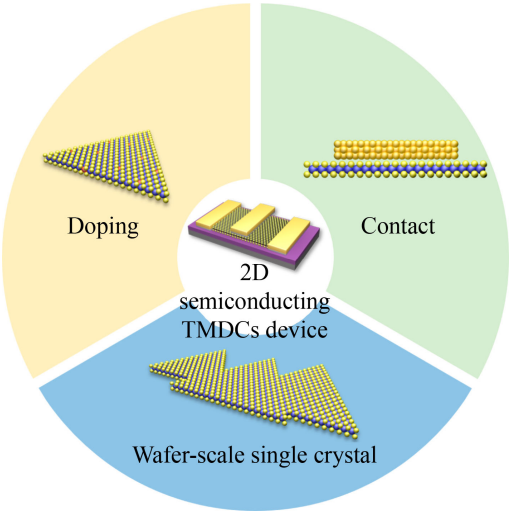

Keywords 2D semiconductor, transition metal dichalcogenides, wafer-scale single crystal, ingenious doping, interfacial contact, device performance

Contents

Higher Education Press

https://doi.org/10.1007/s11467-022-1190-1

1 Introduction

Recent years have witnessed the great breakthrough of semiconductor technology due to the introduction of silicon transistors [1]. Following the Moore's law, the number of transistors in chips is exponentially increasing and the device performances are improved significantly, in consideration of the continuous miniaturization of silicon-based process nodes [2, 3]. However, the Moore's law is becoming unsustainable due to the physical limits of bulk silicon materials, the short-channel effects and high heat dissipation phenomena are inevitably appeared, and further reducing the size of silicon-based field-effect transistors (FETs) is facing a major challenge [4]. In this context, two-dimensional (2D) materials, such as graphene [5, 6], boron nitride [7, 8], and transition metal dichalcogenides (TMDCs) [9, 10], have attracted extensive attention due to their novel physical properties and excellent device performances, such as anomalous Hall effect [11], room temperature quantum Hall effect [12], ultrahigh carrier mobility [13], excellent thermal conductivity [14], and light transmission [15]. The sizes of FETs can be further reduced by replacing the silicon channels with 2D materials [16, 17].

As a unique member of 2D materials, the semiconducting TMDCs have exhibited great potentials in the state-of-the-art FETs [18]. The layered structure allows the channel to be thinned to the monolayer and exhibits excellent electrostatic control capacity, and thus the operating voltage/current and energy consumption can be reduced effectively [19, 20]. The smooth surface without dangling bond reduces the degradation of carrier mobility induced by the scattering [21, 22]. The abundant band structure enables the design of novel logic and memory device [23, 24]. For example, by using the exfoliated few-layer and monolayer MoS_2 nanosheets as the channels, the ultrahigh electron mobility (~34 000 $cm^2 \cdot V^{-1} \cdot s^{-1}$) [25] and excellent on/off current ratio (~10^8) [26] was obtained, respectively. The ultralow contact resistance (~0.2 $k\Omega \cdot \mu m$) was achieved in monolayer MoS_2 transistor by constructing the 1T-2H MoS_2 lateral heterostructure [27]. By using a physically assembled silicon nanowire as the lift-off mask, the ultrashort channel device with few-layer MoS_2 channel was created and showed remarkable conduction current density (~0.83 $mA \cdot \mu m^{-1}$) at room temperature [28]. The abovementioned results reveal that the 2D semiconducting TMDCs offer a promising playground for the construction of high performance electronic devices.

However, the device performances of 2D semiconducting TMDCs are still unsatisfactory, and which are limited by the following bottlenecks. First, the intrinsic defects (e.g., vacancies, grain boundaries, and impurities, etc.) in 2D TMDCs increase the carrier scattering sites and reduce the device performances [29–32]. Second, although the band structures of 2D TMDCs can be modulated and new physical phenomena can be introduced by means of a doping strategy [33–37], the excessive doping should bring in the deep impurity levels and reduce the device performances [38, 39]. Third, the difference between the work function of metal electrodes and the electronic affinity energy of 2D semiconducting TMDCs results in high Schottky barrier height and contact resistance [40–43]. Therefore, the controlled synthesis of high-quality samples with few defects, the development of ingenious doping strategy, and the optimization design of interfacial contacts between electrodes and channels are crucial for improving the device performances of 2D semiconducting TMDCs.

This article hereby aims to provide an up-to-date summary or discussion on the aforementioned issues as described in Fig. 1. Specifically, the chemical vapor deposition (CVD) synthesis of wafer-scale 2D semiconducting TMDCs single crystals will be introduced, and the internal mechanisms will be discussed. The accurate doping of 2D semiconducting TMDCs by the metal atoms and organic molecules will be reviewed. Furthermore, some new methods including the electrode transfer, the introduction of semimetal electrodes, and the construction of 2D metallic/semiconducting TMDCs heterostructures will also be summarized to optimize the interfacial contact.

2 Controllable synthesis of wafer-scale 2D semiconducting TMDCs single crystals

The ultrahigh carrier mobility, excellent on/off current ratio, and distinguished subthreshold swing of 2D semiconducting TMDCs provide a wide application prospect

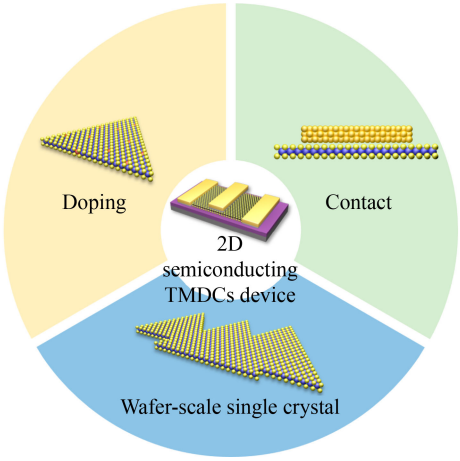

Fig. 1 Three strategies for improving the device performances of 2D semiconducting TMDCs.

in the high performance electronic devices [5, 44–46]. However, the presence of grain boundaries in polycrystalline TMDCs films increases the carrier scattering sites and reduces the carrier mobilities and conductance [47–49]. Therefore, controllable synthesis of wafer-scale 2D semiconducting TMDCs single crystals is essential for the electronic device applications. Recently, fruitful achievements have been attained in growing 2D single crystals [50–56]. For example, inch-sized graphene single crystals were synthesized on Cu–Ni alloys by controlling the nucleation [50]. Through the seamless stitching of unidirectional domains, wafer-scale 2D single crystals were obtained, such as graphene on Ge(110) [51], h-BN on liquid Au substrate [54], vicinal Cu(110) [55], and Cu(111)/sapphire [56]. Notably, there are two distinct routes for synthesizing wafer-scale 2D single crystals: (i) the nucleation controlling: allowing only one nucleation site on a wafer-scale substrate, and then the single nucleus further grows to a wafer-scale single crystal; (ii) the orientation controlling: a substantial number of unidirectional domains epitaxially grow on a single-crystalline substrate, and further generate a wafer-scale single crystal by the seamlessly stitching [57].

2.1 Synthesis of 2D semiconducting TMDCs single crystals by the nucleation controlling

The nucleation controlling is extremely difficult for synthesizing wafer-scale 2D semiconducting TMDCs single crystals in view of the complicated growth kinetics. Nevertheless, the phase transition design is a plausible method to solve such an issue. Xu *et al.* [58] developed a solid-to-solid phase transition and recrystallization strategy to grow 2D semiconducting 2H-$MoTe_2$ single crystals on amorphous insulating substrates. As illustrated in Fig. 2(a), a single-crystalline 2H-$MoTe_2$ nanoflake was deliberately implanted on the center of 1T′-$MoTe_2$ wafer and used as the seed crystal to trigger the phase transition and recrystallization. Subsequently, a dense Al_2O_3 film (~30 nm) was deposited on the wafer to isolate the 1T′-$MoTe_2$ from Te precursors and prevent the random nucleation of 2H-$MoTe_2$. A small hole was introduced into the seed region and served as the only channel of Te precursors supply.

Notably, during the annealing process, the Te vacancies were reduced and the rearrangement of Mo and Te atoms of the bottom 1T′-$MoTe_2$ layers triggered the transition from 1T′ to 2H phase. The lattice structures, crystal orientations, and stacking orders of the bottom $MoTe_2$ were identical to the seed crystal after the recrystallization process, as proved by the aberration-corrected scanning transmission electron microscopy (AC-STEM) in Fig. 2(b). Interestingly, with increasing the annealing time, the phase transition expanded to the outside seed regions and then the wafer-scale 2H-$MoTe_2$ single crystal was formed, as shown in Figs. 2(c) and (d). In addition, a large-scale coplanar heterophase of 1T′/2H/1T′-$MoTe_2$ FET arrays were then fabricated to verify the device performance uniformity of such a single crystal film [Fig. 2(e)]. As shown in Figs. 2(f) and (g), the excellent room temperature carrier mobility (45 ± 2 $cm^2 \cdot V^{-1} \cdot s^{-1}$) and on/off current ratio [$(1.8 \pm 0.3) \times 10^4$] were obtained, comparable to the reported values of single-crystalline 2H-$MoTe_2$ nanoflake transistors. And such results suggested the ultrahigh device performance and its spatial uniformity of 2H-$MoTe_2$ single crystal [59, 60].

In short, the phase transition design provides an innovative route for synthesizing wafer-scale 2D semiconducting 2H-$MoTe_2$ single crystals. However, the uniform and atomically flat few-layer 1T′-$MoTe_2$ film is required to serve as the precursor of phase transition, and it is difficult to synthesize monolayer 2H-$MoTe_2$ single crystal. Moreover, this method is also inapplicable for the growth of other 2D TMDCs with large energy differences between different phases.

2.2 Synthesis of 2D semiconducting TMDCs single crystals by the orientation controlling

The orientation controlling was proven to be a reasonable method for the direct synthesis of wafer-scale 2D single crystals [51, 54]. However, it remains challenging to obtain the unidirectional domains of 2D TMDCs due to the symmetry mismatch between TMDCs and substrate [57]. Chen *et al.* [61] proposed that the parallel steps of sapphire (0001) surfaces could be served as the nucleation sites of monolayer WS_2 and further induced the formation of unidirectional alignment domains. Recently, Li *et al.* [62] realized the epitaxial growth of 2-inch monolayer MoS_2 single crystal on a *c*-plane sapphire with a miscut angle towards *a*-axis. As presented in Figs. 3(a) and(b), the parallel steps of *c*/*a* sapphire were used as the nucleation sites for growing monolayer MoS_2 with unidirectional alignments and single crystal films [Figs. 3(c) and (d)].

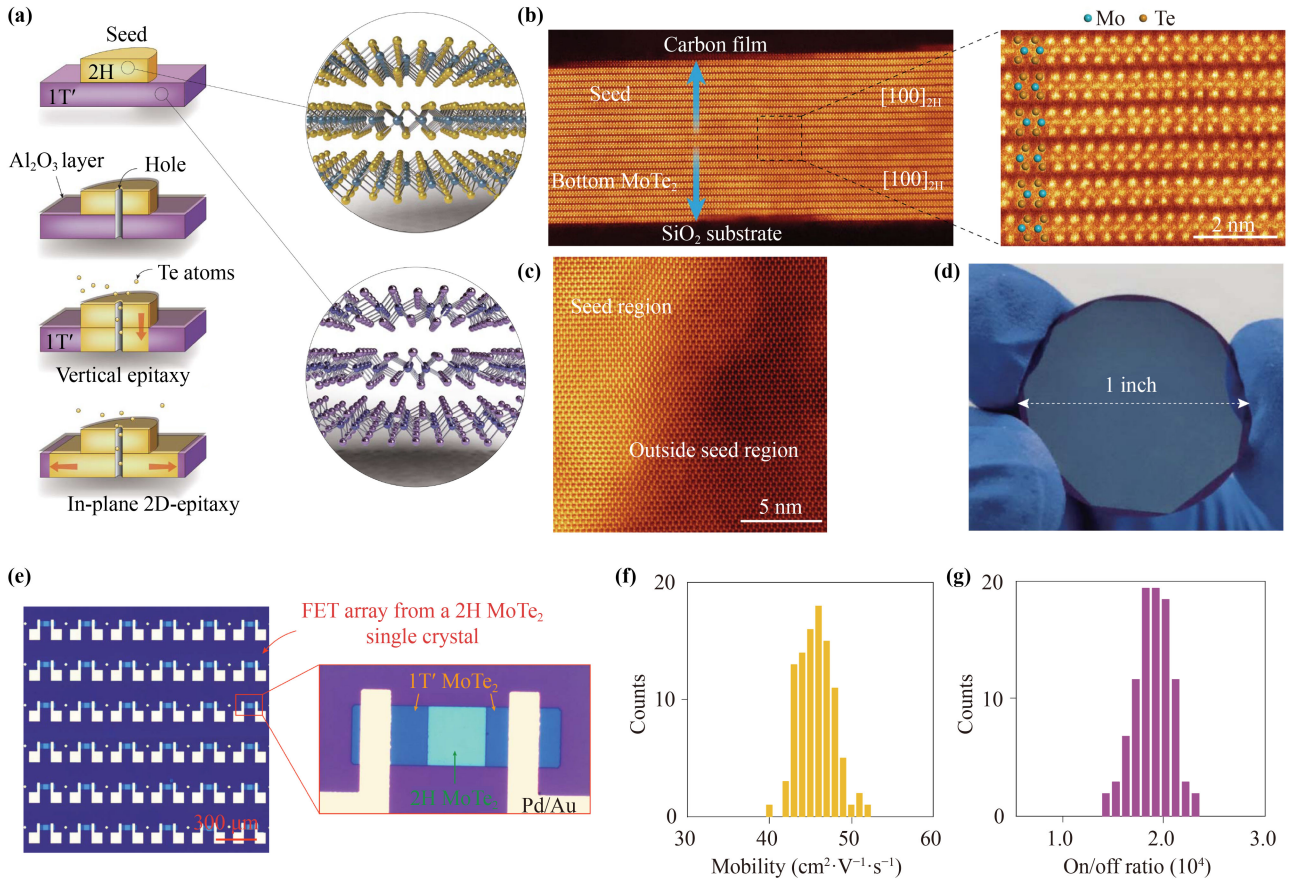

Fig. 2 The nucleation controlling method for synthesizing wafer-scale 2D semiconducting TMDCs single crystals. **(a)** Schematic diagram of the seed growth of wafer-scale 2H-$MoTe_2$ single crystal [58]. **(b)** Cross-section STEM image of the seed region [58]. **(c)** HAADF-STEM image captured from the seed edge [58]. **(d)** Photograph of the 1-inch 2H-$MoTe_2$ single crystal [58]. **(e)** Optical image of the coplanar heterophase of 1T′/2H/1T′-$MoTe_2$ FET arrays [58]. **(f, g)** Statistical distribution of the field-effect mobility and on/off current ratio of 2H-$MoTe_2$ FETs [58].

The first-principles calculations were then performed to clarify the growth mechanism, as revealed in Fig. 3(e). The presence of parallel steps lowered the symmetry of *c*-plane sapphire and broke the degeneracy of formation energy of two possible edge configurations (ZZ–Mo–S_2 and ZZ–S_2), which resulted in the most energetically favorable configuration of ZZ–Mo–S_2 for the unidirectional growth of monolayer MoS_2. Furthermore, the monolayer MoS_2 FET arrays were also fabricated to evaluate the device performance and its uniformity, as presented in Fig. 3(f). The statistical results of 151 monolayer FETs showed that both the carrier mobilities and subthreshold swings subjected to the Gaussian distribution with the variation of ~15% and ~11%, respectively, suggested the high device performance uniformity of wafer-scale monolayer MoS_2 single crystal [Fig. 3(g)]. The average and maximum carrier mobility was obtained to be ~77.6 and ~102.6 $cm^2 \cdot V^{-1} \cdot s^{-1}$, respectively, much higher than that of the monolayer polycrystalline MoS_2 film [63, 64]. Notably, the terrace height of sapphire substrate is also crucial for synthesizing wafer-scale bilayer MoS_2 [65, 66].

In addition, as shown in Fig. 3(h), the orientation controlling method was also employed to synthesize wafer-scale monolayer WS_2 single crystals on vicinal *a*-plane sapphire [67]. The low-energy electron diffraction (LEED) pattern captured from different regions of WS_2 films showed two sets of 3-fold symmetry spots with different diffraction intensities [Fig. 3(i)], confirmed the formation of monolayer WS_2 single crystal. Furthermore, the parallelly aligned holes with hexagonal shapes were generated on monolayer WS_2 film during the oxygen etching process, reconfirmed the epitaxial growth behavior and seamless stitching of misorientation-free WS_2 domains on the vicinal *a*-plane sapphire [Fig. 3(j)]. Besides the step-guided strategy, the other methods were also proposed to regulate the orientations of 2D semiconducting TMDCs and synthesize the wafer-scale single crystals. For example, the parallelly aligned monolayer MoS_2 domains were formed as increased the S/Mo precursor ratio, in view of the complete sulfurization of Mo precursors [68, 69]. In addition, the growth temperature is also crucial for growing wafer-scale 2D semiconducting TMDCs single crystals, and the high temperature results in the undulation of step alignment and the misorientation of TMDCs domains [70].

In short, by the nucleation and orientation controlling,

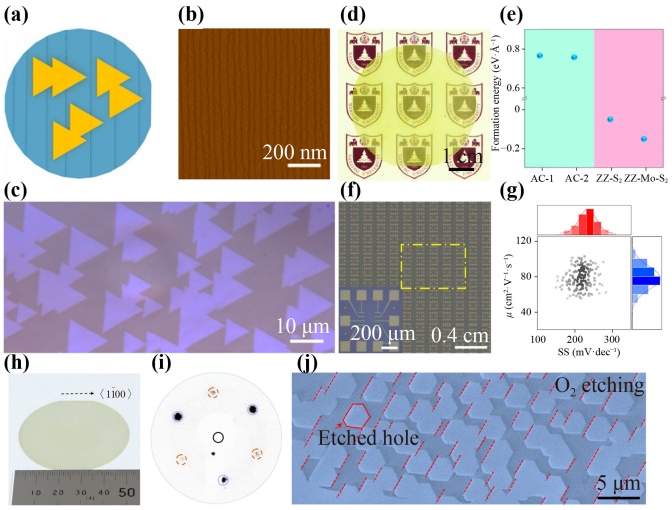

Fig. 3 The orientation controlling method for synthesizing wafer-scale 2D semiconducting TMDCs single crystals. **(a)** Step orientation on c/a sapphire wafer and the corresponding epitaxially aligned MoS_2 domains [62]. **(b)** AFM image of an annealed c/a sapphire [62]. **(c)** Optical image of MoS_2 domains on c/a sapphire [62]. **(d)** Photography of the 2-inch monolayer MoS_2 single crystal on c/a sapphire [62]. **(e)** Calculated formation energy of different edge configurations [62]. **(f)** Optical image of monolayer MoS_2 FET arrays [62]. **(g)** Statistical distribution of carrier mobilities and subthreshold swings [62]. **(h)** Photography of the 2-inch monolayer WS_2 single crystal on vicinal a-plane sapphire [67]. **(i)** Corresponding LEED pattern [67]. **(j)** SEM image of the as-grown WS_2 film after O_2 etching [67].

the wafer-scale 2D semiconducting TMDCs (e.g., MoS_2, WS_2, 2H-$MoTe_2$) single crystals have been successfully synthesized and which lays the solid foundation for constructing high performance electronic devices. Nevertheless, the controlled growth of 2D semiconducting single crystals remains challenging, such as the complicated growth process of phase transition and recrystallization, as well as the expensive growth substrates of c/a and a-plane sapphire.

3 The accurate doping of 2D semiconducting TMDCs

The controlled doping of 2D semiconductors is an important strategy for modulating their electronic properties and introducing novel physical phenomena [71–74]. For example, the band structure, carrier density, and photoluminescence intensity of 2D semiconducting TMDCs can be tuned by means of accurate doping. However, the excessive doping should introduce the deep impurity levels and reduce the device performances [38, 39]. In this section, we will summarize the recent experimental advances regarding the accurate doping of 2D semiconducting TMDCs and its influence on the device performances.

3.1 The Fe-doping of monolayer MoS_2

As a type of interesting dopants, the magnetic transition metal atoms (e.g., Fe, Co, and Mn, etc.) could introduce the novel physical phenomena in 2D TMDCs [75–78]. Recently, Li *et al.* [79] reported the CVD synthesis of large-area monolayer Fe-doped MoS_2 on SiO_2/Si. As shown in Fig. 4(a), the monolayer Fe-doped MoS_2 triangles were obtained with the maximum domain size of ~250 μm. Notably, the Fermi level of monolayer MoS_2 was moved toward the conduction band minimum (CBM) after the Fe doping due to the additional bands from s and p orbitals of Fe, indicated the n-type doping behavior, as revealed in Fig. 4(b).

To evaluate the device performance, the monolayer Fe-doped MoS_2 FETs were thus constructed by using Cr/Au as the electrodes. Excellent room temperature on/off current ratio and electron mobility (~10^8 and ~54 $cm^2 \cdot V^{-1} \cdot s^{-1}$) were obtained for monolayer Fe-doped MoS_2, much higher than those of the pristine monolayer MoS_2 (~10^7 and ~6 $cm^2 \cdot V^{-1} \cdot s^{-1}$), suggested the enhanced device performance. Furthermore, the contact resistance was also extracted by using the transfer length method (TLM), as shown in Fig. 4(c). The contact resistance of monolayer Fe-doped MoS_2 was calculated as ~678 Ω·μm, much smaller than that of the pristine monolayer MoS_2

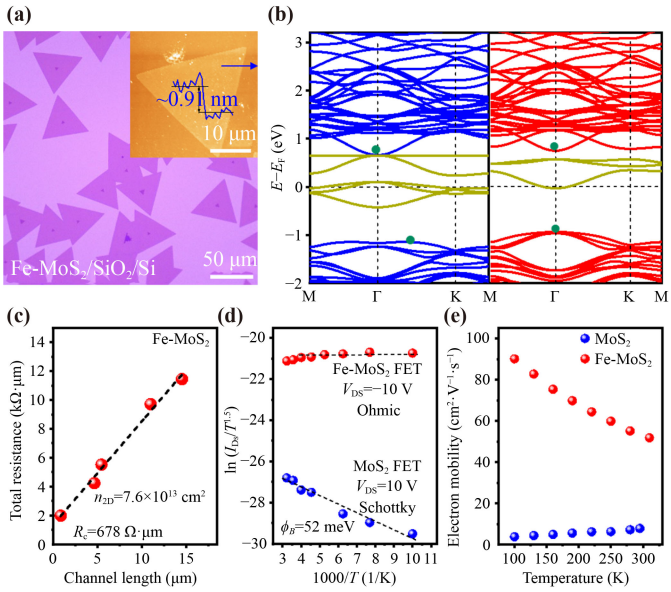

Fig. 4 The Fe-doping of CVD-synthesized monolayer MoS_2. **(a)** Optical microscopy and atomic force microscopy images of CVD-synthesized monolayer Fe-doped MoS_2 on SiO_2/Si [79]. **(b)** Band structures of monolayer Fe-doped MoS_2 with spin-up (left) and spin-down bands (right) [79]. **(c)** Contact resistance extraction of monolayer Fe-doped MoS_2 by using TLM [79]. **(d)** Arrhenius plots of the Ohmic-contacted Fe-doped MoS_2 and Schottky-contact MoS_2 devices [79]. **(e)** Electron mobility evolution of monolayer Fe-doped MoS_2 and pristine monolayer MoS_2 devices as a function of temperature [79].

(~117 kΩ·μm), indicated the outstanding interfacial contacts between monolayer Fe-doped MoS_2 and electrodes. To clarify the internal mechanism, the temperature-dependent electrical measurements were thus performed. The energy barriers of monolayer Fe-doped MoS_2 and pristine monolayer MoS_2 were extracted from the Arrhenius plots in Fig. 4(d), and the perfect Ohmic contact was confirmed for Fe-doped MoS_2. Furthermore, the enhanced electron mobility was also observed in monolayer Fe-doped MoS_2 as the temperature decreasing from ~300 K to ~100 K, indicated the suppressed ionized impurity scattering [Fig. 4(e)]. Such results reveal that the device performances of 2D semiconducting TMDCs can be improved by the accurate Fe doping, and which provides a new scheme for downscaling the electronic devices.

3.2 The remote modulation doping of few layer MoS_2 by triphenylphosphine

Although the doping is required for modulating the electronic properties of semiconductors, the introduction of impurities should result in the Coulomb scattering and hinders the charge transport, especially for 2D semiconductors. To avoid this issue, a remote modulation doping strategy was developed in the WSe_2/h-BN/MoS_2 heterostructures [80]. The triphenylphosphine (PPh_3) was selected as the dopants and then imposed on the top layers of WSe_2 [Fig. 5(a)]. Notably, the electrons from PPh_3 were introduced into WSe_2 layers through the molecular doping and spontaneously transferred to MoS_2 layers in view of the conduction band offset, which resulted in the n-type doping in MoS_2 channel, as shown in Fig. 5(b).

To verify the doping capability of PPh_3, the electrical measurements of modulation-doped (MD) WSe_2/h-BN/MoS_2 and directly doped (DD) MoS_2 FETs were performed. The negative shifts of threshold voltages were clearly observed for both MoS_2 devices after the PPh_3 treatments, indicated the n-type doping behavior, as shown in Fig. 5(c). The same variation tendency was also demonstrated in the electron density, which suggested that the PPh_3 molecules could modulate the carrier density of underlying MoS_2 channels through the remote charge transfer across the WSe_2/h-BN layers without a substantial loss in the doping efficiency. Notably, the electron densities of such two type MoS_2 devices could be tuned by the doping concentrations and treatment time. In addition, the carrier mobility of MoS_2 in MD device remained unchanged at ~60 $cm^2 \cdot V^{-1} \cdot s^{-1}$, even after the electron doping. Nevertheless, a degraded mobility from ~60 $cm^2 \cdot V^{-1} \cdot s^{-1}$ to ~35 $cm^2 \cdot V^{-1} \cdot s^{-1}$ was obviously observed for the DD counterparts [Fig. 5(d)]. Such results suggested that the charged impurity scattering was suppressed through the remote modulation doping strategy.

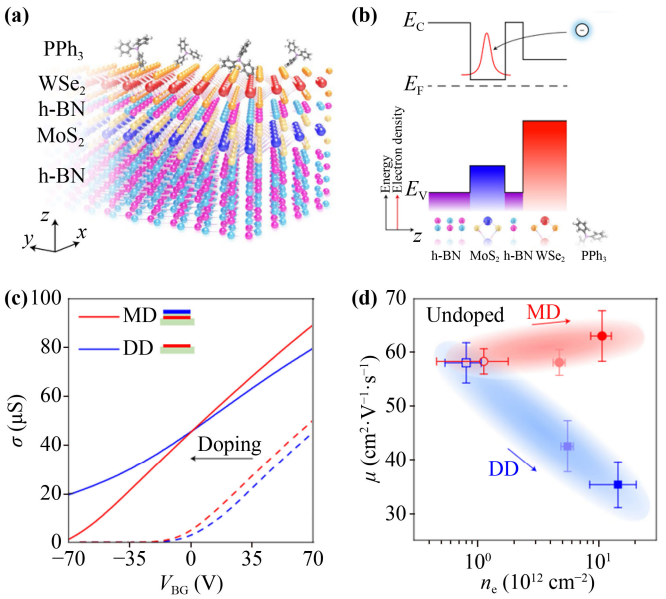

Fig. 5 The remote modulation doping of few-layer MoS_2 by triphenylphosphine. **(a)** Schematic diagram of the representative WSe_2/h-BN/MoS_2 heterostructures [80]. **(b)** Band diagram of the doped WSe_2/h-BN/MoS_2 FET [80]. **(c)** Gate voltage dependent electrical sheet conductivity of MD and DD MoS_2 FETs before (dashed lines) and after (solid lines) PPh_3 doping [80]. **(d)** Electron concentration dependent carrier mobility before (open symbols) and after (filled symbols) PPh_3 doping [80].

3.3 The photo-induced and electrostatic doping strategies of 2D TMDCs

In addition, the other doping methods, such as the photo-induced and electrostatic doping, have also been proposed in 2D TMDCs. For example, Seo *et al.* [72] reported a reversible photo-induced doping of few-layer 2H-$MoTe_2$ and 2H-WSe_2 as revealed in Figs. 6(a)–(c), and the polarity of channel was reconfigured from n-type to p-type under the different laser light frequencies. The light-lattice interactions, as well as the self-interstitial defects of Te under ultraviolet illumination and the subsequent substitutions of O in Te/Mo vacancies under visible illumination resulted in the reconfigurable doping effect. By using such a method, the complementary metal-oxide-semiconductor (CMOS) device on a single channel was also constructed, and the circuit functions were dynamically reset from the inverter to the switch under the different light frequencies, as shown in Fig. 6(d). Furthermore, Wang *et al.* [81] reported an electrostatic-doping-driven phase transition between the hexagonal and monoclinic phases of monolayer $MoTe_2$, as demonstrated in Fig. 6(e) and proved by the hysteretic loop in Raman spectra [Fig. 6(f)]. The electrostatic doping method opens up a new possibility for the construction of phase-change devices at the atomic scale.

Briefly, the band structures and electronic properties of 2D semiconducting TMDCs can be modulated by

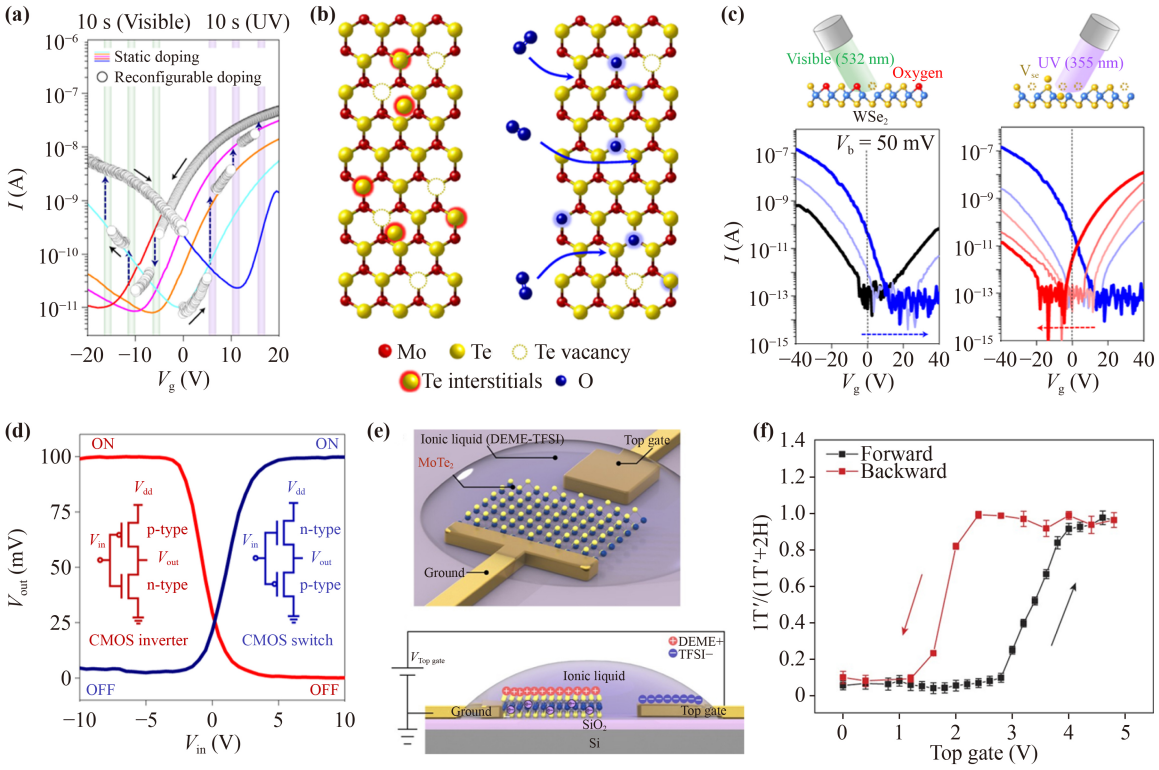

Fig. 6 Photo-induced and electrostatic doping strategy of 2D TMDCs. **(a)** Transfer characteristics of reconfigurable doping on few-layer 2H-$MoTe_2$ [72]. **(b)** Schematic diagram of the in-plane crystal structures of few-layer 2H-$MoTe_2$ [72]. **(c)** Schematics diagram of the selective doping and corresponding transfer characteristics of few-layer 2H-WSe_2 [72]. **(d)** Transfer characteristics of CMOS inverter [72]. **(e)** Schematic diagram and measurement configuration of a monolayer $MoTe_2$ transistor [81]. **(f)** Gate-dependent Raman intensity ratios [81].

means of ingenious doping, and which provides a new paradigm for improving the device performances and extending the Moore's law. However, the internal mechanism of metal doping should be further explored and the stability of remote modulation doping should also be enhanced.

4 The optimization design of interfacial contacts between electrodes and 2D semiconducting channels

The optimization design of interfacial contacts between electrodes and channels is crucial for realizing the applications of 2D semiconductors in high performance electronic and optoelectronic devices [41, 43, 82– 84]. Notably, the interfacial contact quality can be evaluated by the contact resistance. For example, the low contact resistance is crucial for achieving high "on" current density, large photoresponse, and high-frequency operation [85]. Nevertheless, the difference between the work function of metal electrodes and the electronic affinity energy of 2D semiconducting TMDCs results in the formation of Schottky barrier [86]. Furthermore, the Fermi-level pinning effect is also induced by the disorder-induced gap state (DIGS) and metal-induced gap state (MIGS) [87], which breaks the Schottky–Mott rule. Therefore, the optimization design of interfacial contacts is significant for improving the device performances of 2D semiconducting TMDCs. In this section, we will review three methods to optimize the interfacial contacts including the electrode transfer, the introduction of semimetal electrodes, and the construction of 2D metallic/semiconducting TMDCs heterostructures.

4.1 The electrode transfer for improving the device performances of 2D semiconducting TMDCs

The defects and disorders should be introduced on the surfaces of 2D semiconducting TMDCs during the lithography and thermal evaporation processes, which degenerate the device performances accordingly. Notably, the van der Waals contacts between electrodes and 2D semiconductors without Fermi-level pinning are theoretically possible. For example, the clean interfaces were created in the van der Waals metal–semiconductor junctions by laminating the metal electrodes with atomically flat surfaces onto the dangling-bond-free 2D

semiconductors, as shown in Fig. 7(a) [88]. The excellent device performances (with the electron and hole mobility up to ~260 and ~175 $cm^2 \cdot V^{-1} \cdot s^{-1}$, respectively) were clearly observed in the exfoliated few-layer MoS_2 by using the transferred Ag and Pt electrodes [Figs. 7(b), (c)]. Furthermore, the S factor, which was characterized the Fermi level pin strength, was obtained to be ~0.96 for the devices with transferred metal electrodes, approached to the Schottky–Mott law limit defined by the electrostatic energy alignment. On the contrary, the S factor was calculated as ~0.09 for the control devices with evaporated metal electrodes, indicated strong Fermi-level pinning effect near the CBM at the electrode/MoS_2 interfaces, as demonstrated in Fig. 7(d). Such an interesting electrode transfer establishes a highly efficient and damage-free strategy for constructing high performance electronic devices.

In addition, the interaction- and defect-free van der Waals contacts were formed between the metal electrodes and exfoliated few-layer WSe_2 nanosheets via a metal deposition process that used the Se buffer layer [89]. In detail, the Se layer was used to protect the WSe_2 channel during the metal evaporation process and it could be removed by the annealing process at ~150 ℃ [Fig. 7(e)]. The n-type behavior was clearly observed for the direct Au contacted few-layer WSe_2 device, in view of the Fermi-level pinning effect near the conduction band at the Au–WSe_2 interface. However, the p-type characteristic with a large on/off current ratio ($>10^6$) and high hole mobility (~135 $cm^2 \cdot V^{-1} \cdot s^{-1}$) was presented in the van der Waals contacted few-layer WSe_2 due to the perfect interface [Fig. 7(f)]. Density functional theory (DFT) calculations were then performed to understand the band structure at the Au–WSe_2 interface [Figs. 7(g), (h)]. The new states were formed in the mid-bandgap region of the direct Au contact WSe_2, and changed the band bending direction. Nevertheless, the density of states (DOS) of WSe_2 were formed in the van der Waals contact with Au electrodes and exhibited few mid-gap states. The construction of van der Waals contact using a Se buffer layer provides new route for controlling the Schottky barrier height and can be used for fabricating the large-scale electronic devices.

4.2 The introduction of semimetal electrodes for improving the device performances of 2D semiconducting TMDCs

The Fermi-level pinning effect can be suppressed by constructing van der Waals contact, nevertheless, the tunneling barriers are inevitable because of the interface gaps between electrodes and channels. In addition, the electrode transfer process should be implemented in a sufficiently clean environment, therefore, this approach is vulnerable to the external influence and difficult to apply to industrially relevant large-substrate technology. Herein, the exploitation of new electrode materials is necessary.

Notably, as the semiconductor closed to a metal surface, the extended wavefunction of metal perturbed the environment of semiconductor and resulted in the emergence of MIGS [Fig. 8(a)], totally different from the initial state of semiconductor [Fig. 8(c)] [90]. Specially, if the Fermi level of electrode lied inside the semiconductor bandgap, the Schottky barrier was thus formed unavoidably. However, for the semimetal Bi electrode, the zero DOS near the Fermi level induced few MIGS.

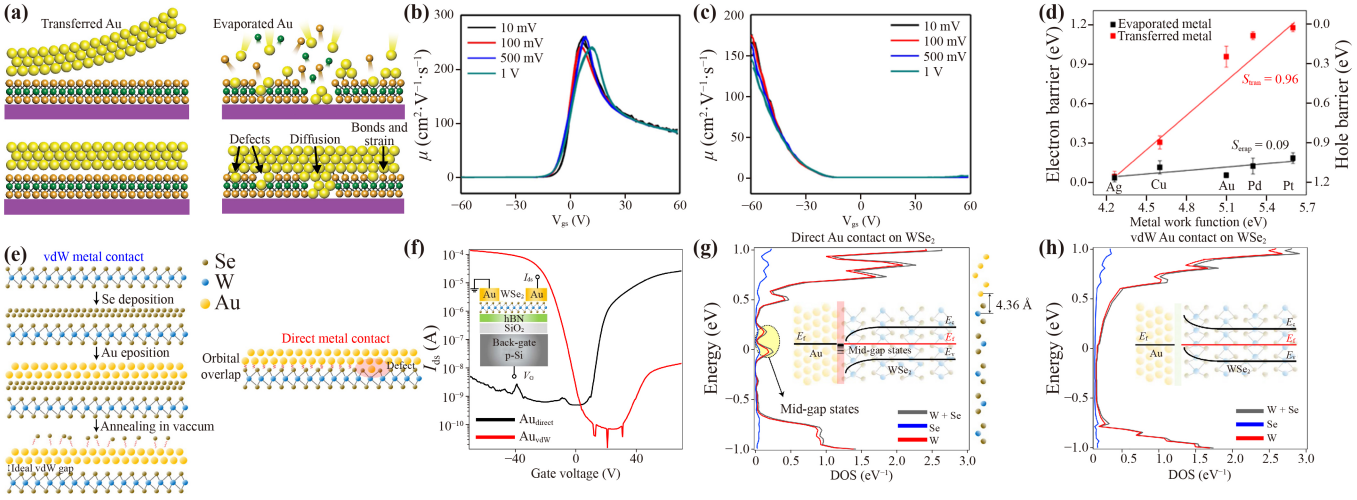

Fig. 7 The electrode transfer method for improving the device performances of 2D semiconducting TMDCs. **(a)** Schematic diagram of the transferred and deposited Au electrodes on MoS_2 [88]. **(b, c)** Electron and hole mobility of few-layer MoS_2 by using the transferred Ag and Pt electrodes [88]. **(d)** Schottky barrier height of few-layer MoS_2 by using different transferred and evaporated electrodes [88]. **(e)** Schematic diagram of the van der Waals and direct Au contacted few-layer WSe_2 [89]. **(f)** Transfer curve of few-layer WSe_2 with the van der Waals and direct Au contact, respectively [89]. **(g, h)** DFT calculation results of WSe_2 with the van der Waals and direct Au contact, respectively [89].

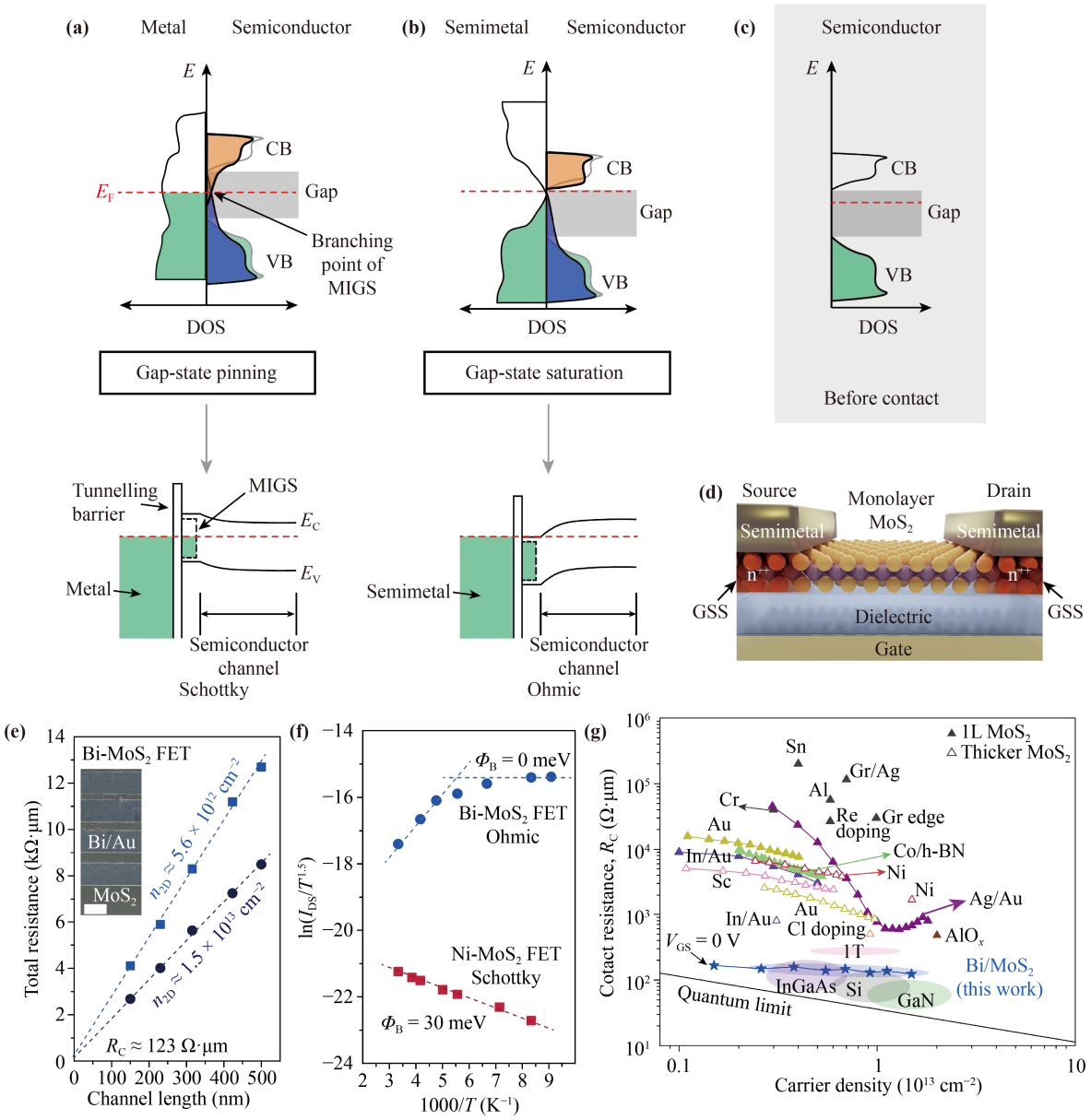

Fig. 8 The introduction of semimetal electrodes for improving the device performances of 2D semiconducting TMDCs. **(a)** DOS of normal metal and semiconductor contact, and the corresponding band structure [90]. **(b)** DOS of semimetal and semiconductor contact, and the corresponding band structure [90]. **(c)** The reference DOS of semiconductor before contact [90]. **(d)** Schematic diagram of a monolayer MoS_2 FET with Bi contact [90]. **(e)** Contact resistance of Bi-MoS_2 FETs extraction by using the TLM [90]. **(f)** Arrhenius plots of the Ohmic Bi-MoS_2 and Schottky Ni-MoS_2 FETs at the carrier density of 1.5×10^{12} cm^{-2} [90]. **(g)** The state-of-the-art contact technology of MoS_2 FETs plotted as a function of carrier density [90].

Particularly, its Fermi level closed to the CBM of monolayer MoS_2, and the conduction-band-contributed MIGS were greatly suppressed [Fig. 8(b)]. As a result, the degenerate state and free of Schottky barrier at the interface were formed as the semimetal Bi contacted monolayer MoS_2. The schematic diagram of monolayer MoS_2 back-gated FET with Bi contact was shown in Fig. 8(d). The ultralow contact resistance (~123 Ω·μm at the carrier density of 1.5×10^{13} cm^{-2}) and zero Schottky barrier height was obtained, respectively, as revealed in Figs. 8(e) and (f), indicated the ultrahigh device performance of Bi contacted monolayer MoS_2. Notably, the contact resistance values were comparable to those of three-dimensional semiconductors, and approached to the quantum limit [Fig. 8(g)]. Even so, in view of the low work function of Bi electrode, it is incapable to reduce the Schottky barrier height of hole. Therefore, searching for high work function semimetal electrodes is crucial for fabricating high performance p-type devices.

4.3 The construction of 2D metallic/semiconducting TMDCs heterostructures

2D metallic TMDCs have attracted great attention due

to their interesting physical properties (e.g., charge density waves order, superconductivity, and magnetism, etc.) [91–108]. In addition, some revolutionary applications such as transparent electrodes and energy conversion/storage have also explored in the 2D metallic TMDCs, by virtue of the ultrahigh conductivities, excellent electrocatalytic activities, and novel layered structures [109–124]. Notably, the 2D metallic TMDCs are considered as ideal electrode materials for improving the device performances of 2D semiconducting TMDCs in view of their similar atomic structures and complementary electronic properties [27, 59, 125–133].

The VS_2–MoS_2 lateral heterostructures were successfully synthesized on SiO_2/Si by a two-step CVD method, as revealed in Figs. 9(a) and (b) [134]. The back-gate monolayer MoS_2 FETs were then fabricated with the lateral VS_2 and vertical Ni contact, respectively [Fig. 9(c)]. The contact resistances of such two typical monolayer MoS_2 devices were extracted by the four-probe measurements and plotted in Fig. 9(d). Notably, the contact resistance of VS_2–MoS_2 was obtained to be ~520 Ω·μm, more than ten times smaller than that of Ni-MoS_2 contacts (~8640 Ω·μm) [Fig. 9(d)], indicated the perfect interfacial contact. Furthermore, the 2D metallic/semiconducting TMDCs heterostructure arrays were also CVD synthesized by using a focused laser irradiation and raster scan method, as shown in Fig. 9(e) [135]. The VSe_2/WSe_2 heterostructure array FETs were thus constructed [Fig. 9(f)], and demonstrated ultrahigh device performances with the mobility of ~135 $cm^2 \cdot V^{-1} \cdot s^{-1}$, much higher than that of Cr/Au contacted monolayer WSe_2 (~10 $cm^2 \cdot V^{-1} \cdot s^{-1}$), which was attributed to the protective effect of VSe_2 on the monolayer WSe_2 channel during the electrode evaporation process [Fig. 9(g)].

5 Conclusion and perspectives

2D semiconducting TMDCs have shown great application potentials in the electronic devices due to their novel physical properties, atomically thin thicknesses, and abundant band structures. However, the device performances are still lower than that of the theoretical values, which is attributed to the intrinsic defects, excessive doping, and daunting contacts. From these perspectives, we have summarized three strategies for improving the device performances of 2D semiconducting TMDCs, including (i) the synthesis of wafer-scale 2D semiconducting TMDCs single crystals by the nucleation and orientation controlling to reduce the grain boundary densities, (ii) the accurate doping of 2D semiconducting TMDCs by the metal atoms and remote modulations to tune the band structures and suppress the impurity scatterings of 2D semiconducting TMDCs, and (iii) the optimization design of interfacial contacts between electrodes and 2D semiconducting TMDCs channels by means of transferring metal electrodes, introducing semimetal electrodes, and constructing 2D metallic/semiconducting TMDCs heterostructures.

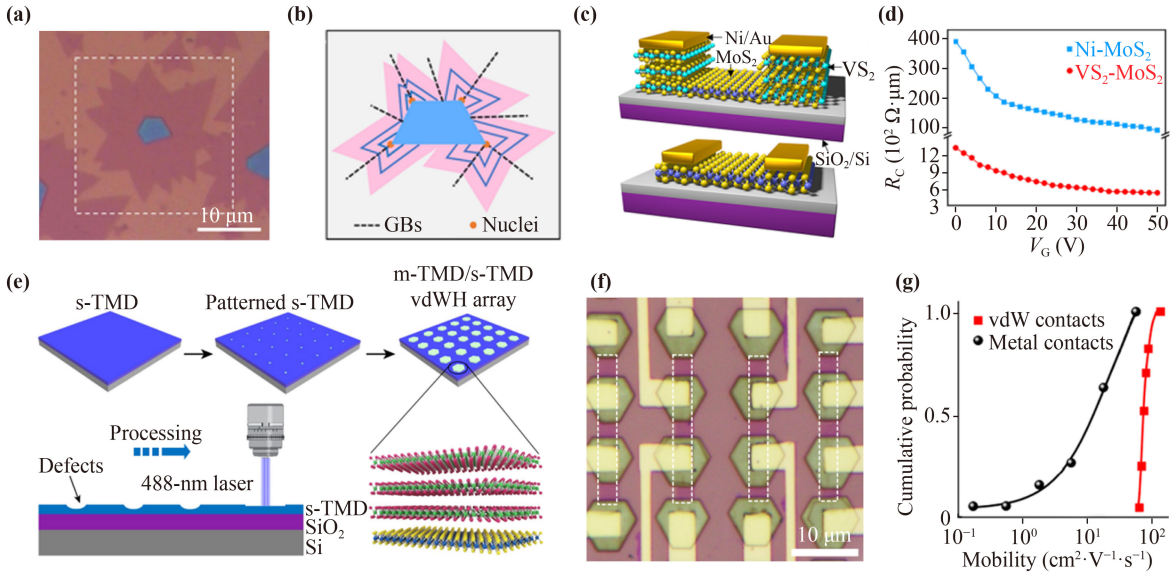

Fig. 9 The construction of 2D metallic/semiconducting TMDCs heterostructures for improving the device performances. **(a)** Optical image of the MoS_2-VS_2 lateral heterostructure [134]. **(b)** Schematic illustration of the stitching growth mechanism of monolayer MoS_2 [134]. **(c)** Schematic diagram of the monolayer MoS_2 FETs with the lateral VS_2 (upper) and vertical Ni contacts (lower) [134]. **(d)** Contact resistances of monolayer MoS_2 FETs with the VS_2 and Ni contacts [134]. **(e)** The growth process of 2D metallic/semiconducting TMDCs heterostructure arrays [135]. **(f)** Optical image of back-gated WSe_2 transistors with the VSe_2 contacts [135]. **(g)** Carrier mobility distribution of monolayer WSe_2 transistors with the VSe_2 and Cr/Au contacts [135].

Although the impressive achievements have been made in such aspects, some daunting challenges are still unresolved. For the synthesis of wafer-scale 2D semiconducting TMDCs single crystals, the high-cost sapphire substrates with a small miscut angle are used for controlling the domain orientations. Moreover, the long-time pretreatment of substrates at extremely high temperature is needed before the synthesis of 2D TMDCs. Thus, it is urgent to develop a facile technology for growing wafer-scale 2D semiconducting TMDCs single crystals on the commercially available substrates. For the controllable doping, the organic molecules are unstable in the atmosphere, and which are incompatible with the device construction. Furthermore, the intrinsic mechanism of metal doping is still unclear, and more experimental and theoretical explorations are required. For the optimization design of interfacial contact, the electrode transfer method is complicated, and the gap between electrode and channel will introduce the tunneling barrier. In addition, the small work function of semimetal electrode is disadvantageous to reduce the Schottky barrier height of p-type semiconductor. The controllable synthesis of wafer-scale 2D metallic/semiconducting TMDCs heterostructures is still unaddressed.

Although there are some challenges, many breakthroughs will be made in the near future regarding the improvement of device performances of 2D semiconducting TMDCs. For instance, the interactions between 2D TMDCs domains and substrates can be tuned by the metal doping during the CVD growth process, and it is feasible to obtain the wafer-scale 2D semiconducting TMDCs single crystals on the commercially available substrates. Meanwhile, the metal doping is also beneficial for modulating the band structures of 2D TMDCs and reducing the contact resistances between electrodes and channels. In addition, some newfangled physical properties, such as magnetism, can be introduced by the metal doping, and which provides a new route for the construction of multifunctional electronic devices.

Acknowledgements This work was supported by the National Key R&D Program of China (Grant Nos. 2018YFA0703700 and 2021YFA1200800), the National Natural Science Foundation of China (Grant Nos. 91964203 and 92164103), the Beijing National Laboratory for Molecular Sciences (Grant No. BNLMS202001), and the Fundamental Research Funds for the Central Universities (Grant No. 2042021kf0029).

References

1. R. W. Keyes, Physical limits of silicon transistors and circuits, *Rep. Prog. Phys.* 68(12), 2701 (2005)
2. M. Buchanan, Generalizing Moore, *Nat. Phys.* 12(3), 200 (2016)
3. S. Lloyd, Ultimate physical limits to computation, *Nature* 406(6799), 1047 (2000)
4. C. Liu, H. Chen, S. Wang, Q. Liu, Y. G. Jiang, D. W. Zhang, M. Liu, and P. Zhou, Two-dimensional materials for next-generation computing technologies, *Nat. Nanotechnol.* 15(7), 545 (2020)
5. M. Chhowalla, D. Jena, and H. Zhang, Two-dimensional semiconductors for transistors, *Nat. Rev. Mater.* 1(11), 16052 (2016)
6. B. W. Liang, W. H. Chang, H. Y. Lin, P. C. Chen, Y. T. Zhang, K. B. Simbulan, K. S. Li, J. H. Chen, C. H. Kuan, and Y. W. Lan, High-frequency graphene base hot-electron transistor, *ACS Nano* 15(4), 6756 (2021)
7. Y. Gong, Z. Q. Xu, D. Li, J. Zhang, I. Aharonovich, and Y. Zhang, Two-dimensional hexagonal boron nitride for building next-generation energy-efficient devices, *ACS Energy Lett.* 6(3), 985 (2021)
8. N. R. Glavin, C. Muratore, M. L. Jespersen, J. Hu, P. T. Hagerty, A. M. Hilton, A. T. Blake, C. A. Grabowski, M. F. Durstock, M. E. McConney, D. M. Hilgefort, T. S. Fisher, and A. A. Voevodin, Amorphous boron nitride: A universal, ultrathin dielectric for 2D nanoelectronics, *Adv. Funct. Mater.* 26(16), 2640 (2016)
9. J. Shi, M. Hong, Z. Zhang, Q. Ji, and Y. Zhang, Physical properties and potential applications of two-dimensional metallic transition metal dichalcogenides, *Coord. Chem. Rev.* 376(1), 1 (2018)
10. P. Wang, Y. Huan, P. Yang, M. Cheng, J. Shi, and Y. Zhang, Controlled syntheses and multifunctional applications of two-dimensional metallic transition metal dichalcogenides, *Acc. Mater. Res.* 2(9), 751 (2021)
11. Y. Zhang, Y. W. Tan, H. L. Stormer, and P. Kim, Experimental observation of the quantum Hall effect and Berry's phase in graphene, *Nature* 438(7065), 201 (2005)
12. K. S. Novoselov, Z. Jiang, Y. Zhang, S. V. Morozov, H. L. Stormer, U. Zeitler, J. C. Maan, G. S. Boebinger, P. Kim, and A. K. Geim, Room-temperature quantum Hall effect in graphene, *Science* 315(5817), 1379 (2007)
13. X. Du, I. Skachko, A. Barker, and E. Y. Andrei, Approaching ballistic transport in suspended graphene, *Nat. Nanotechnol.* 3(8), 491 (2008)
14. H. Seol Jae, I. Jo, L. Moore Arden, L. Lindsay, H. Aitken Zachary, T. Pettes Michael, X. Li, Z. Yao, R. Huang, D. Broido, N. Mingo, S. R. Rodney, and L. Shi, Two-dimensional phonon transport in supported graphene, *Science* 328(5975), 213 (2010)
15. R. R. Nair, P. Blake, A. N. Grigorenko, K. S. Novoselov, T. J. Booth, T. Stauber, N. M. R. Peres, and A. K. Geim, Fine structure constant defines visual transparency of graphene, *Science* 320(5881), 1308 (2008)
16. L. Ju, M. Bie, X. Zhang, X. Chen, and L. Kou, Two-dimensional Janus van der Waals heterojunctions: A review of recent research progresses, *Front. Phys.* 16(1), 13201 (2021)
17. D. Akinwande, C. Huyghebaert, C. H. Wang, M. I. Serna, S. Goossens, L. J. Li, H. S. P. Wong, and F. H. L. Koppens, Graphene and two-dimensional materials for silicon technology, *Nature* 573(7775), 507 (2019)
18. Q. H. Wang, K. Kalantar-Zadeh, A. Kis, J. N. Coleman, and M. S. Strano, Electronics and optoelectronics

of two-dimensional transition metal dichalcogenides, *Nat. Nanotechnol.* 7(11), 699 (2012)
19. C. Tan, Z. Lai, and H. Zhang, Ultrathin two-dimensional multinary layered metal chalcogenide nanomaterials, *Adv. Mater.* 29(37), 1701392 (2017)
20. C. Tan, X. Cao, X. J. Wu, Q. He, J. Yang, X. Zhang, J. Chen, W. Zhao, S. Han, G. H. Nam, M. Sindoro, and H. Zhang, Recent advances in ultrathin two-dimensional nanomaterials, *Chem. Rev.* 117(9), 6225 (2017)
21. Y. Liu, X. Duan, H. J. Shin, S. Park, Y. Huang, and X. Duan, Promises and prospects of two-dimensional transistors, *Nature* 591(7848), 43 (2021)
22. X. Jing, Y. Illarionov, E. Yalon, P. Zhou, T. Grasser, Y. Shi, and M. Lanza, Engineering field effect transistors with 2D semiconducting channels: Status and prospects, *Adv. Funct. Mater.* 30(18), 1901971 (2020)
23. Q. Zeng, H. Wang, W. Fu, Y. Gong, W. Zhou, P. M. Ajayan, J. Lou, and Z. Liu, Band engineering for novel two-dimensional atomic layers, *Small* 11(16), 1868 (2015)
24. X. Bao, Q. Ou, Z. Q. Xu, Y. Zhang, Q. Bao, and H. Zhang, Band structure engineering in 2D materials for optoelectronic applications, *Adv. Mater. Technol.* 3(11), 1800072 (2018)
25. X. Cui, G. H. Lee, Y. D. Kim, G. Arefe, P. Y. Huang, C. H. Lee, D. A. Chenet, X. Zhang, L. Wang, F. Ye, F. Pizzocchero, B. S. Jessen, K. Watanabe, T. Taniguchi, D. A. Muller, T. Low, P. Kim, and J. Hone, Multi-terminal transport measurements of MoS_2 using a van der Waals heterostructure device platform, *Nat. Nanotechnol.* 10(6), 534 (2015)
26. B. Radisavljevic, A. Radenovic, J. Brivio, V. Giacometti, and A. Kis, Single-layer MoS_2 transistors, *Nat. Nanotechnol.* 6(3), 147 (2011)
27. R. Kappera, D. Voiry, S. E. Yalcin, B. Branch, G. Gupta, A. D. Mohite, and M. Chhowalla, Phase-engineered low-resistance contacts for ultrathin MoS_2 transistors, *Nat. Mater.* 13(12), 1128 (2014)
28. Y. Liu, J. Guo, Y. Wu, E. Zhu, N. O. Weiss, Q. He, H. Wu, H. C. Cheng, Y. Xu, I. Shakir, Y. Huang, and X. Duan, Pushing the performance limit of sub-100 nm molybdenum disulfide transistors, *Nano Lett.* 16(10), 6337 (2016)
29. Z. Hu, Z. Wu, C. Han, J. He, Z. Ni, and W. Chen, Two-dimensional transition metal dichalcogenides: Interface and defect engineering, *Chem. Soc. Rev.* 47(9), 3100 (2018)
30. S. Najmaei, Z. Liu, W. Zhou, X. Zou, G. Shi, S. Lei, B. I. Yakobson, J. C. Idrobo, P. M. Ajayan, and J. Lou, Vapour phase growth and grain boundary structure of molybdenum disulphide atomic layers, *Nat. Mater.* 12(8), 754 (2013)
31. D. Rhodes, S. H. Chae, R. Ribeiro-Palau, and J. Hone, Disorder in van der Waals heterostructures of 2D materials, *Nat. Mater.* 18(6), 541 (2019)
32. H. Qiu, T. Xu, Z. Wang, W. Ren, H. Nan, Z. Ni, Q. Chen, S. Yuan, F. Miao, F. Song, G. Long, Y. Shi, L. Sun, J. Wang, and X. Wang, Hopping transport through defect-induced localized states in molybdenum disulphide, *Nat. Commun.* 4(1), 2642 (2013)
33. S. H. Ryu, M. Huh, D. Y. Park, C. Jozwiak, E. Rotenberg, A. Bostwick, and K. S. Kim, Pseudogap in a crystalline insulator doped by disordered metals, *Nature* 596(7870), 68 (2021)
34. J. Suh, T. L. Tan, W. Zhao, J. Park, D. Y. Lin, T. E. Park, J. Kim, C. Jin, N. Saigal, S. Ghosh, Z. M. Wong, Y. Chen, F. Wang, W. Walukiewicz, G. Eda, and J. Wu, Reconfiguring crystal and electronic structures of MoS_2 by substitutional doping, *Nat. Commun.* 9(1), 199 (2018)
35. V. Kochat, A. Apte, J. A. Hachtel, H. Kumazoe, A. Krishnamoorthy, S. Susarla, J. C. Idrobo, F. Shimojo, P. Vashishta, R. Kalia, A. Nakano, C. S. Tiwary, and P. M. Ajayan, Re doping in 2D transition metal dichalcogenides as a new route to tailor structural phases and induced magnetism, *Adv. Mater.* 29(43), 1703754 (2017)
36. S. Fu, K. Kang, K. Shayan, A. Yoshimura, S. Dadras, X. Wang, L. Zhang, S. Chen, N. Liu, A. Jindal, X. Li, A. N. Pasupathy, A. N. Vamivakas, V. Meunier, S. Strauf, and E. H. Yang, Enabling room temperature ferromagnetism in monolayer MoS_2 via *in situ* iron-doping, *Nat. Commun.* 11(1), 2034 (2020)
37. S. M. Hus, R. Ge, P. A. Chen, L. Liang, G. E. Donnelly, W. Ko, F. Huang, M. H. Chiang, A. P. Li, and D. Akinwande, Observation of single-defect memristor in an MoS_2 atomic sheet, *Nat. Nanotechnol.* 16(1), 58 (2021)
38. S. Wang, A. Robertson, and J. H. Warner, Atomic structure of defects and dopants in 2D layered transition metal dichalcogenides, *Chem. Soc. Rev.* 47(17), 6764 (2018)
39. J. Y. Noh, H. Kim, M. Park, and Y. S. Kim, Deep-to-shallow level transition of Re and Nb dopants in monolayer MoS_2 with dielectric environments, *Phys. Rev. B* 92(11), 115431 (2015)
40. S. Chen, S. Wang, C. Wang, Z. Wang, and Q. Liu, Latest advance on seamless metal–semiconductor contact with ultralow Schottky barrier in 2D-material-based devices, *Nano Today* 42, 101372 (2022)
41. Y. Wang and M. Chhowalla, Making clean electrical contacts on 2D transition metal dichalcogenides, *Nat. Rev. Phys.* 4(2), 101 (2022)
42. X. Zhang, B. Liu, L. Gao, H. Yu, X. Liu, J. Du, J. Xiao, Y. Liu, L. Gu, Q. Liao, Z. Kang, Z. Zhang, and Y. Zhang, Near-ideal van der Waals rectifiers based on all-two-dimensional Schottky junctions, *Nat. Commun.* 12(1), 1522 (2021)
43. X. Zheng, A. Calò, E. Albisetti, X. Liu, A. S. M. Alharbi, G. Arefe, X. Liu, M. Spieser, W. J. Yoo, T. Taniguchi, K. Watanabe, C. Aruta, A. Ciarrocchi, A. Kis, B. S. Lee, M. Lipson, J. Hone, D. Shahrjerdi, and E. Riedo, Patterning metal contacts on monolayer MoS_2 with vanishing Schottky barriers using thermal nanolithography, *Nat. Electron.* 2(1), 17 (2019)
44. S. Manzeli, D. Ovchinnikov, D. Pasquier, O. V. Yazyev, and A. Kis, 2D transition metal dichalcogenides, *Nat. Rev. Mater.* 2(8), 17033 (2017)
45. Y. Liu, N. O. Weiss, X. Duan, H. C. Cheng, Y. Huang, and X. Duan, Van der Waals heterostructures and devices, *Nat. Rev. Mater.* 1(9), 16042 (2016)

46. G. Fiori, F. Bonaccorso, G. Iannaccone, T. Palacios, D. Neumaier, A. Seabaugh, S. K. Banerjee, and L. Colombo, Electronics based on two-dimensional materials, *Nat. Nanotechnol.* 9(10), 768 (2014)
47. A. M. van der Zande, P. Y. Huang, D. A. Chenet, T. C. Berkelbach, Y. M. You, G. H. Lee, T. F. Heinz, D. R. Reichman, D. A. Muller, and J. C. Hone, Grains and grain boundaries in highly crystalline monolayer molybdenum disulphide, *Nat. Mater.* 12(6), 554 (2013)
48. T. H. Ly, D. J. Perello, J. Zhao, Q. M. Deng, H. Kim, G. H. Han, S. H. Chae, H. Y. Jeong, and Y. H. Lee, Misorientation-angle-dependent electrical transport across molybdenum disulfide grain boundaries, *Nat. Commun.* 7(1), 10426 (2016)
49. H. G. Ji, Y. C. Lin, K. Nagashio, M. Maruyama, P. Solís-Fernández, A. Sukma Aji, V. Panchal, S. Okada, K. Suenaga, and H. Ago, Hydrogen-assisted epitaxial growth of monolayer tungsten disulfide and seamless grain stitching, *Chem. Mater.* 30(2), 403 (2018)
50. T. Wu, X. Zhang, Q. Yuan, J. Xue, G. Lu, Z. Liu, H. Wang, H. Wang, F. Ding, Q. Yu, X. Xie, and M. Jiang, Fast growth of inch-sized single-crystalline graphene from a controlled single nucleus on Cu–Ni alloys, *Nat. Mater.* 15(1), 43 (2016)
51. J. H. Lee, E. K. Lee, W. J. Joo, Y. Jang, B. S. Kim, J. Y. Lim, S. H. Choi, S. J. Ahn, J. R. Ahn, M. H. Park, C. W. Yang, B. L. Choi, S. W. Hwang, and D. Whang, Wafer-scale growth of single-crystal monolayer graphene on reusable hydrogen-terminated germanium, *Science* 344(6181), 286 (2014)
52. M. Huang, P. V. Bakharev, Z. J. Wang, M. Biswal, Z. Yang, S. Jin, B. Wang, H. J. Park, Y. Li, D. Qu, Y. Kwon, X. Chen, S. H. Lee, M. G. Willinger, W. J. Yoo, Z. Lee, and R. S. Ruoff, Large-area single-crystal AB-bilayer and ABA-trilayer graphene grown on a Cu/Ni(111) foil, *Nat. Nanotechnol.* 15(4), 289 (2020)
53. M. Wang, M. Huang, D. Luo, Y. Li, M. Choe, W. K. Seong, M. Kim, S. Jin, M. Wang, S. Chatterjee, Y. Kwon, Z. Lee, and R. S. Ruoff, Single-crystal, large-area, fold-free monolayer graphene, *Nature* 596(7873), 519 (2021)
54. J. S. Lee, S. H. Choi, S. J. Yun, Y. I. Kim, S. Boandoh, J. H. Park, B. G. Shin, H. Ko, S. H. Lee, Y. M. Kim, Y. H. Lee, K. K. Kim, and S. M. Kim, Wafer-scale single-crystal hexagonal boron nitride film via self-collimated grain formation, *Science* 362(6416), 817 (2018)
55. L. Wang, X. Xu, L. Zhang, R. Qiao, M. Wu, Z. Wang, S. Zhang, J. Liang, Z. Zhang, Z. Zhang, W. Chen, X. Xie, J. Zong, Y. Shan, Y. Guo, M. Willinger, H. Wu, Q. Li, W. Wang, P. Gao, S. Wu, Y. Zhang, Y. Jiang, D. Yu, E. Wang, X. Bai, Z. J. Wang, F. Ding, and K. Liu, Epitaxial growth of a 100-square-centimetre single-crystal hexagonal boron nitride monolayer on copper, *Nature* 570(7759), 91 (2019)
56. T. A. Chen, C. P. Chuu, C. C. Tseng, C. K. Wen, H. S. P. Wong, S. Pan, R. Li, T. A. Chao, W. C. Chueh, Y. Zhang, Q. Fu, B. I. Yakobson, W. H. Chang, and L. J. Li, Wafer-scale single-crystal hexagonal boron nitride monolayers on Cu(111), *Nature* 579(7798), 219 (2020)
57. L. Zhang, J. Dong, and F. Ding, Strategies, status, and challenges in wafer scale single crystalline two-dimensional materials synthesis, *Chem. Rev.* 121(11), 6321 (2021)
58. X. Xu, Y. Pan, S. Liu, B. Han, P. Gu, S. Li, W. Xu, Y. Peng, Z. Han, J. Chen, P. Gao, and Y. Ye, Seeded 2D epitaxy of large-area single-crystal films of the van der Waals semiconductor 2H $MoTe_2$, *Science* 372(6538), 195 (2021)
59. S. Cho, S. Kim, J. H. Kim, J. Zhao, J. Seok, D. H. Keum, J. Baik, D. H. Choe, K. J. Chang, K. Suenaga, S. W. Kim, Y. H. Lee, and H. Yang, Phase patterning for ohmic homojunction contact in $MoTe_2$, *Science* 349(6248), 625 (2015)
60. J. H. Sung, H. Heo, S. Si, Y. H. Kim, H. R. Noh, K. Song, J. Kim, C. S. Lee, S. Y. Seo, D. H. Kim, H. K. Kim, H. W. Yeom, T. H. Kim, S. Y. Choi, J. S. Kim, and M. H. Jo, Coplanar semiconductor–metal circuitry defined on few-layer $MoTe_2$ via polymorphic heteroepitaxy, *Nat. Nanotechnol.* 12(11), 1064 (2017)
61. L. Chen, B. Liu, M. Ge, Y. Ma, A. N. Abbas, and C. Zhou, Step-edge-guided nucleation and growth of aligned WSe_2 on sapphire via a layer-over-layer growth mode, *ACS Nano* 9(8), 8368 (2015)
62. T. Li, W. Guo, L. Ma, W. Li, Z. Yu, Z. Han, S. Gao, L. Liu, D. Fan, Z. Wang, Y. Yang, W. Lin, Z. Luo, X. Chen, N. Dai, X. Tu, D. Pan, Y. Yao, P. Wang, Y. Nie, J. Wang, Y. Shi, and X. Wang, Epitaxial growth of wafer-scale molybdenum disulfide semiconductor single crystals on sapphire, *Nat. Nanotechnol.* 16(11), 1201 (2021)
63. H. Yu, M. Liao, W. Zhao, G. Liu, X. Zhou, Z. Wei, X. Xu, K. Liu, Z. Hu, K. Deng, S. Zhou, J. A. Shi, L. Gu, C. Shen, T. Zhang, L. Du, L. Xie, J. Zhu, W. Chen, R. Yang, D. Shi, and G. Zhang, Wafer-scale growth and transfer of highly-oriented monolayer MoS_2 continuous films, *ACS Nano* 11(12), 12001 (2017)
64. K. K. H. Smithe, S. V. Suryavanshi, M. Muñoz Rojo, A. D. Tedjarati, and E. Pop, Low variability in synthetic monolayer MoS_2 devices, *ACS Nano* 11(8), 8456 (2017)
65. R. Dong, X. Gong, J. Yang, Y. Sun, L. Ma, and J. Wang, The intrinsic thermodynamic difficulty and a step-guided mechanism for the epitaxial growth of uniform multilayer MoS_2 with controllable thickness, *Adv. Mater.* 34(20), 2201402 (2022)
66. L. Liu, T. Li, L. Ma, W. Li, S. Gao, W. Sun, R. Dong, X. Zou, D. Fan, L. Shao, C. Gu, N. Dai, Z. Yu, X. Chen, X. Tu, Y. Nie, P. Wang, J. Wang, Y. Shi, and X. Wang, Uniform nucleation and epitaxy of bilayer molybdenum disulfide on sapphire, *Nature* 605(7908), 69 (2022)
67. J. Wang, X. Xu, T. Cheng, L. Gu, R. Qiao, Z. Liang, D. Ding, H. Hong, P. Zheng, Z. Zhang, Z. Zhang, S. Zhang, G. Cui, C. Chang, C. Huang, J. Qi, J. Liang, C. Liu, Y. Zuo, G. Xue, X. Fang, J. Tian, M. Wu, Y. Guo, Z. Yao, Q. Jiao, L. Liu, P. Gao, Q. Li, R. Yang, G. Zhang, Z. Tang, D. Yu, E. Wang, J. Lu, Y. Zhao, S. Wu, F. Ding, and K. Liu, Dual-coupling-guided epitaxial growth of wafer-scale single-crystal WS_2 monolayer on vicinal *a*-plane sapphire, *Nat. Nanotechnol.* 17(1), 33 (2022)
68. P. Yang, S. Zhang, S. Pan, B. Tang, Y. Liang, X. Zhao, Z. Zhang, J. Shi, Y. Huan, Y. Shi, S. J.

Pennycook, Z. Ren, G. Zhang, Q. Chen, X. Zou, Z. Liu, and Y. Zhang, Epitaxial growth of centimeter-scale single-crystal MoS_2 monolayer on Au(111), *ACS Nano* 14(4), 5036 (2020)
69. A. Aljarb, Z. Cao, H. Tang, J. Huang, M. Li, W. Hu, L. Cavallo, and L. Li, Substrate lattice-guided seed formation controls the orientation of 2D transition-metal dichalcogenides, *ACS Nano* 11(9), 9215 (2017)
70. M. Chubarov, T. H. Choudhury, D. R. Hickey, S. Bachu, T. Zhang, A. Sebastian, A. Bansal, H. Zhu, N. Trainor, S. Das, M. Terrones, N. Alem, and J. M. Redwing, Wafer-scale epitaxial growth of unidirectional WS_2 monolayers on sapphire, *ACS Nano* 15(2), 2532 (2021)
71. T. Shinada, S. Okamoto, T. Kobayashi, and I. Ohdomari, Enhancing semiconductor device performance using ordered dopant arrays, *Nature* 437(7062), 1128 (2005)
72. S. Y. Seo, G. Moon, O. F. N. Okello, M. Y. Park, C. Han, S. Cha, H. Choi, H. W. Yeom, S. Y. Choi, J. Park, and M. H. Jo, Reconfigurable photo-induced doping of two-dimensional van der Waals semiconductors using different photon energies, *Nat. Electron.* 4(1), 38 (2021)
73. Y. H. Chen, R. R. Tamming, K. Chen, Z. Zhang, F. Liu, Y. Zhang, J. M. Hodgkiss, R. J. Blaikie, B. Ding, and M. Qiu, Bandgap control in two-dimensional semiconductors *via* coherent doping of plasmonic hot electrons, *Nat. Commun.* 12(1), 4332 (2021)
74. J. Zhou, H. Zhu, Q. Song, Z. Ding, J. Mao, Z. Ren, and G. Chen, Mobility enhancement in heavily doped semiconductors via electron cloaking, *Nat. Commun.* 13(1), 2482 (2022)
75. B. Li, T. Xing, M. Zhong, L. Huang, N. Lei, J. Zhang, J. Li, and Z. Wei, A two-dimensional Fe-doped SnS_2 magnetic semiconductor, *Nat. Commun.* 8(1), 1958 (2017)
76. J. Zhou, J. Lin, H. Sims, C. Jiang, C. Cong, J. A. Brehm, Z. Zhang, L. Niu, Y. Chen, Y. Zhou, Y. Wang, F. Liu, C. Zhu, T. Yu, K. Suenaga, R. Mishra, S. T. Pantelides, Z. G. Zhu, W. Gao, Z. Liu, and W. Zhou, Synthesis of Co-doped MoS_2 monolayers with enhanced valley splitting, *Adv. Mater.* 32(11), 1906536 (2020)
77. Q. Li, X. Zhao, L. Deng, Z. Shi, S. Liu, Q. Wei, L. Zhang, Y. Cheng, L. Zhang, H. Lu, W. Gao, W. Huang, C. W. Qiu, G. Xiang, S. J. Pennycook, Q. Xiong, K. Loh, and B. Peng, Enhanced valley Zeeman splitting in Fe-doped monolayer MoS_2, *ACS Nano* 14(4), 4636 (2020)
78. K. Zhang, S. Feng, J. Wang, A. Azcatl, N. Lu, R. Addou, N. Wang, C. Zhou, J. Lerach, V. Bojan, M. J. Kim, L. Q. Chen, R. M. Wallace, M. Terrones, J. Zhu, and J. A. Robinson, Manganese doping of monolayer MoS_2: The substrate is critical, *Nano Lett.* 15(10), 6586 (2015)
79. H. Li, M. Cheng, P. Wang, R. Du, L. Song, J. He, and J. Shi, Reducing contact resistance and boosting device performance of monolayer MoS_2 by *in situ* Fe doping, *Adv. Mater.* 34(18), 2200885 (2022)
80. D. Lee, J. J. Lee, Y. S. Kim, Y. H. Kim, J. C. Kim, W. Huh, J. Lee, S. Park, H. Y. Jeong, Y. D. Kim, and C. H. Lee, Remote modulation doping in van der Waals heterostructure transistors, *Nat. Electron.* 4(9), 664 (2021)
81. Y. Wang, J. Xiao, H. Zhu, Y. Li, Y. Alsaid, K. Y. Fong, Y. Zhou, S. Wang, W. Shi, Y. Wang, A. Zettl, E. J. Reed, and X. Zhang, Structural phase transition in monolayer $MoTe_2$ driven by electrostatic doping, *Nature* 550(7677), 487 (2017)
82. S. Song, Y. Sim, S. Y. Kim, J. H. Kim, I. Oh, W. Na, D. H. Lee, J. Wang, S. Yan, Y. Liu, J. Kwak, J. H. Chen, H. Cheong, J. W. Yoo, Z. Lee, and S. Y. Kwon, Wafer-scale production of patterned transition metal ditelluride layers for two-dimensional metal–semiconductor contacts at the Schottky–Mott limit, *Nat. Electron.* 3(4), 207 (2020)
83. Y. Jung, M. S. Choi, A. Nipane, A. Borah, B. Kim, A. Zangiabadi, T. Taniguchi, K. Watanabe, W. J. Yoo, J. Hone, and J. T. Teherani, Transferred via contacts as a platform for ideal two-dimensional transistors, *Nat. Electron.* 2(5), 187 (2019)
84. W. Liu, Transition metal ditellurides make for better 2D contacts, *Nat. Electron.* 3(4), 187 (2020)
85. A. Allain, J. Kang, K. Banerjee, and A. Kis, Electrical contacts to two-dimensional semiconductors, *Nat. Mater.* 14(12), 1195 (2015)
86. R. T. Tung, The physics and chemistry of the Schottky barrier height, *Appl. Phys. Rev.* 1(1), 011304 (2014)
87. X. Liu, M. S. Choi, E. Hwang, W. J. Yoo, and J. Sun, Fermi level pinning dependent 2D semiconductor devices: Challenges and prospects, *Adv. Mater.* 34(15), 2108425 (2022)
88. Y. Liu, J. Guo, E. Zhu, L. Liao, S. J. Lee, M. Ding, I. Shakir, V. Gambin, Y. Huang, and X. Duan, Approaching the Schottky–Mott limit in van der Waals metal–semiconductor junctions, *Nature* 557(7707), 696 (2018)
89. G. Kwon, Y. H. Choi, H. Lee, H. S. Kim, J. Jeong, K. Jeong, M. Baik, H. Kwon, J. Ahn, E. Lee, and M. H. Cho, Interaction- and defect-free van der Waals contacts between metals and two-dimensional semiconductors, *Nat. Electron.* 5(4), 241 (2022)
90. P. C. Shen, C. Su, Y. Lin, A. S. Chou, C. C. Cheng, J. H. Park, M. H. Chiu, A. Y. Lu, H. L. Tang, M. M. Tavakoli, G. Pitner, X. Ji, Z. Cai, N. Mao, J. Wang, V. Tung, J. Li, J. Bokor, A. Zettl, C. I. Wu, T. Palacios, L. J. Li, and J. Kong, Ultralow contact resistance between semimetal and monolayer semiconductors, *Nature* 593(7858), 211 (2021)
91. J. Shi, X. Wang, S. Zhang, L. Xiao, Y. Huan, Y. Gong, Z. Zhang, Y. Li, X. Zhou, M. Hong, Q. Fang, Q. Zhang, X. Liu, L. Gu, Z. Liu, and Y. Zhang, Two-dimensional metallic tantalum disulfide as a hydrogen evolution catalyst, *Nat. Commun.* 8(1), 958 (2017)
92. J. Shi, X. Chen, L. Zhao, Y. Gong, M. Hong, Y. Huan, Z. Zhang, P. Yang, Y. Li, Q. Zhang, Q. Zhang, L. Gu, H. Chen, J. Wang, S. Deng, N. Xu, and Y. Zhang, Chemical vapor deposition grown wafer-scale 2D tantalum diselenide with robust charge-density-wave order, *Adv. Mater.* 30(44), 1804616 (2021)
93. J. Ge, T. Luo, Z. Lin, J. Shi, Y. Liu, P. Wang, Y. Zhang, W. Duan, and J. Wang, Magnetic moments

induced by atomic vacancies in transition metal dichalcogenide flakes, *Adv. Mater.* 33(4), 2005465 (2018)

94. M. Bonilla, S. Kolekar, Y. Ma, H. C. Diaz, V. Kalappattil, R. Das, T. Eggers, H. R. Gutierrez, M. H. Phan, and M. Batzill, Strong room-temperature ferromagnetism in VSe_2 monolayers on van der Waals substrates, *Nat. Nanotechnol.* 13(4), 289 (2018)
95. K. Zhao, H. Lin, X. Xiao, W. Huang, W. Yao, M. Yan, Y. Xing, Q. Zhang, Z. X. Li, S. Hoshino, J. Wang, S. Zhou, L. Gu, M. S. Bahramy, H. Yao, N. Nagaosa, Q. K. Xue, K. T. Law, X. Chen, and S. H. Ji, Disorder-induced multifractal superconductivity in monolayer niobium dichalcogenides, *Nat. Phys.* 15(9), 904 (2019)
96. Y. Xing, P. Yang, J. Ge, J. Yan, J. Luo, H. Ji, Z. Yang, Y. Li, Z. Wang, Y. Liu, F. Yang, P. Qiu, C. Xi, M. Tian, Y. Liu, X. Lin, and J. Wang, Extrinsic and intrinsic anomalous metallic states in transition metal dichalcogenide Ising superconductors, *Nano Lett.* 21(18), 7486 (2021)
97. Z. Wang, Y. Y. Sun, I. Abdelwahab, L. Cao, W. Yu, H. Ju, J. Zhu, W. Fu, L. Chu, H. Xu, and K. P. Loh, Surface-limited superconducting phase transition on 1T-TaS_2, *ACS Nano* 12(12), 12619 (2018)
98. J. Hall, N. Ehlen, J. Berges, E. van Loon, C. van Efferen, C. Murray, M. Rösner, J. Li, B. V. Senkovskiy, M. Hell, M. Rolf, T. Heider, M. C. Asensio, J. Avila, L. Plucinski, T. Wehling, A. Grüneis, and T. Michely, Environmental control of charge density wave order in monolayer 2H-TaS_2, *ACS Nano* 13(9), 10210 (2019)
99. C. Zhu, Y. Chen, F. Liu, S. Zheng, X. Li, A. Chaturvedi, J. Zhou, Q. Fu, Y. He, Q. Zeng, H. J. Fan, H. Zhang, W. J. Liu, T. Yu, and Z. Liu, Light-tunable 1T-TaS_2 charge-density-wave oscillators, *ACS Nano* 12(11), 11203 (2018)
100. J. Bekaert, E. Khestanova, D. G. Hopkinson, J. Birkbeck, N. Clark, M. Zhu, D. A. Bandurin, R. Gorbachev, S. Fairclough, Y. Zou, M. Hamer, D. J. Terry, J. J. P. Peters, A. M. Sanchez, B. Partoens, S. J. Haigh, M. V. Milošević, and I. V. Grigorieva, Enhanced superconductivity in few-layer TaS_2 due to healing by oxygenation, *Nano Lett.* 20(5), 3808 (2020)
101. Y. Chen, L. Wu, H. Xu, C. Cong, S. Li, S. Feng, H. Zhang, C. Zou, J. Shang, S. A. Yang, K. P. Loh, W. Huang, and T. Yu, Visualizing the anomalous charge density wave states in graphene/$NbSe_2$ heterostructures, *Adv. Mater.* 32(45), 2003746 (2020)
102. Q. Dong, J. Pan, S. Li, Y. Fang, T. Lin, S. Liu, B. Liu, Q. Li, F. Huang, and B. Liu, Record-high superconductivity in transition metal dichalcogenides emerged in compressed 2H-TaS_2, *Adv. Mater.* 34(9), 2103168 (2022)
103. W. Zhang, L. Zhang, P. K. J. Wong, J. Yuan, G. Vinai, P. Torelli, G. van der Laan, Y. P. Feng, and A. T. S. Wee, Magnetic transition in monolayer VSe_2 *via* interface hybridization, *ACS Nano* 13(8), 8997 (2019)
104. H. Liu, L. Bao, Z. Zhou, B. Che, R. Zhang, C. Bian, R. Ma, L. Wu, H. Yang, J. Li, C. Gu, C. M. Shen, S. Du, and H. J. Gao, Quasi-2D transport and weak antilocalization effect in few-layered VSe_2, *Nano Lett.* 19(7), 4551 (2019)
105. R. Chua, J. Henke, S. Saha, Y. Huang, J. Gou, X. He, T. Das, J. van Wezel, A. Soumyanarayanan, and A. T. S. Wee, Coexisting charge-ordered states with distinct driving mechanisms in monolayer VSe_2, *ACS Nano* 16(1), 783 (2022)
106. W. Yu, J. Li, T. S. Herng, Z. Wang, X. Zhao, X. Chi, W. Fu, I. Abdelwahab, J. Zhou, J. Dan, Z. Chen, Z. Chen, Z. Li, J. Lu, S. J. Pennycook, Y. P. Feng, J. Ding, and K. P. Loh, Chemically exfoliated VSe_2 monolayers with room-temperature ferromagnetism, *Adv. Mater.* 31(40), 1903779 (2019)
107. Y. Wen, Z. Liu, Y. Zhang, C. Xia, B. Zhai, X. Zhang, G. Zhai, C. Shen, P. He, R. Cheng, L. Yin, Y. Yao, M. Getaye Sendeku, Z. Wang, X. Ye, C. Liu, C. Jiang, C. Shan, Y. Long, and J. He, Tunable room-temperature ferromagnetism in two-dimensional Cr_2Te_3, *Nano Lett.* 20(5), 3130 (2020)
108. Y. Zhang, J. Chu, L. Yin, T. A. Shifa, Z. Cheng, R. Cheng, F. Wang, Y. Wen, X. Zhan, Z. Wang, and J. He, Ultrathin magnetic 2D single-crystal CrSe, *Adv. Mater.* 31(19), 1900056 (2019)
109. X. Zhang, Z. Luo, P. Yu, Y. Cai, Y. Du, D. Wu, S. Gao, C. Tan, Z. Li, M. Ren, T. Osipowicz, S. Chen, Z. Jiang, J. Li, Y. Huang, J. Yang, Y. Chen, C. Y. Ang, Y. Zhao, P. Wang, L. Song, X. Wu, Z. Liu, A. Borgna, and H. Zhang, Lithiation-induced amorphization of $Pd_3P_2S_8$ for highly efficient hydrogen evolution, *Nat. Catal.* 1(6), 460 (2018)
110. Y. Liu, J. Wu, K. P. Hackenberg, J. Zhang, Y. M. Wang, Y. Yang, K. Keyshar, J. Gu, T. Ogitsu, R. Vajtai, J. Lou, P. M. Ajayan, B. C. Wood, and B. I. Yakobson, Self-optimizing, highly surface-active layered metal dichalcogenide catalysts for hydrogen evolution, *Nat. Energy* 2(9), 17127 (2017)
111. J. Yang, A. R. Mohmad, Y. Wang, R. Fullon, X. Song, F. Zhao, I. Bozkurt, M. Augustin, E. J. G. Santos, H. S. Shin, W. Zhang, D. Voiry, H. Y. Jeong, and M. Chhowalla, Ultrahigh-current-density niobium disulfide catalysts for hydrogen evolution, *Nat. Mater.* 18(12), 1309 (2019)
112. M. Yan, X. Pan, P. Wang, F. Chen, L. He, G. Jiang, J. Wang, J. Z. Liu, X. Xu, X. Liao, J. Yang, and L. Mai, Field-effect tuned adsorption dynamics of VSe_2 nanosheets for enhanced hydrogen evolution reaction, *Nano Lett.* 17(7), 4109 (2017)
113. Z. L. Liu, B. Lei, Z. L. Zhu, L. Tao, J. Qi, D. L. Bao, X. Wu, L. Huang, Y. Y. Zhang, X. Lin, Y. L. Wang, S. Du, S. T. Pantelides, and H. J. Gao, Spontaneous formation of 1D pattern in monolayer VSe_2 with dispersive adsorption of Pt atoms for HER catalysis, *Nano Lett.* 19(8), 4897 (2019)
114. I. S. Kwon, I. H. Kwak, T. T. Debela, J. Y. Kim, S. J. Yoo, J. G. Kim, J. Park, and H. S. Kang, Phase-transition $Mo_{1-x}V_xSe_2$ alloy nanosheets with rich V-Se vacancies and their enhanced catalytic performance of hydrogen evolution reaction, *ACS Nano* 15(9), 14672 (2021)
115. Y. Huan, J. Shi, X. Zou, Y. Gong, C. Xie, Z. Yang, Z. Zhang, Y. Gao, Y. Shi, M. Li, P. Yang, S. Jiang, M. Hong, L. Gu, Q. Zhang, X. Yan, and Y. Zhang, Scalable production of two-dimensional metallic transition metal dichalcogenide nanosheet powders using NaCl templates toward electrocatalytic applications, *J. Am.*

Chem. Soc. 141(47), 18694 (2019)

116. C. Yang, J. Feng, F. Lv, J. Zhou, C. Lin, K. Wang, Y. Zhang, Y. Yang, W. Wang, J. Li, and S. Guo, Metallic graphene-like VSe_2 ultrathin nanosheets: Superior potassium-ion storage and their working mechanism, *Adv. Mater.* 30(27), 1800036 (2018)
117. F. Ming, H. Liang, Y. Lei, W. Zhang, and H. N. Alshareef, Solution synthesis of VSe_2 nanosheets and their alkali metal ion storage performance, *Nano Energy* 53, 11 (2018)
118. Q. Yu, Z. Zhang, S. Qiu, Y. Luo, Z. Liu, F. Yang, H. Liu, S. Ge, X. Zou, B. Ding, W. Ren, H. M. Cheng, C. Sun, and B. Liu, A Ta-TaS_2 monolith catalyst with robust and metallic interface for superior hydrogen evolution, *Nat. Commun.* 12(1), 6051 (2021)
119. J. Feng, X. Sun, C. Wu, L. Peng, C. Lin, S. Hu, J. Yang, and Y. Xie, Metallic few-layered VS_2 ultrathin nanosheets: High two-dimensional conductivity for in-plane supercapacitors, *J. Am. Chem. Soc.* 133(44), 17832 (2011)
120. P. He, M. Yan, G. Zhang, R. Sun, L. Chen, Q. An, and L. Mai, Layered VS_2 nanosheet-based aqueous Zn ion battery cathode, *Adv. Energy Mater.* 7(11), 1601920 (2017)
121. J. Zhou, L. Wang, M. Yang, J. Wu, F. Chen, W. Huang, N. Han, H. Ye, F. Zhao, Y. Li, and Y. Li, Hierarchical VS_2 nanosheet assemblies: A universal host material for the reversible storage of alkali metal ions, *Adv. Mater.* 29(35), 1702061 (2017)
122. H. Liang, H. Shi, D. Zhang, F. Ming, R. Wang, J. Zhuo, and Z. Wang, Solution growth of vertical VS_2 nanoplate arrays for electrocatalytic hydrogen evolution, *Chem. Mater.* 28(16), 5587 (2016)
123. S. Zhang, J. Wang, N. L. Torad, W. Xia, M. A. Aslam, Y. V. Kaneti, Z. Hou, Z. Ding, B. Da, A. Fatehmulla, A. M. Aldhafiri, W. A. Farooq, J. Tang, Y. Bando, and Y. Yamauchi, Rational design of nanoporous MoS_2/VS_2 heteroarchitecture for ultrahigh performance ammonia sensors, *Small* 16(12), 1901718 (2020)
124. Y. Zhou, Q. Xu, T. Ge, X. Zheng, L. Zhang, and P. Yan, Accurate control of VS_2 nanosheets for coexisting high photoluminescence and photothermal conversion efficiency, *Angew. Chem. Int. Ed.* 59(8), 3322 (2020)
125. Z. Zhang, Y. Gong, X. Zou, P. Liu, P. Yang, J. Shi, L. Zhao, Q. Zhang, L. Gu, and Y. Zhang, Epitaxial growth of two-dimensional metal–semiconductor transition-metal dichalcogenide vertical stacks (VSe_2/MX_2) and their band alignments, *ACS Nano* 13(1), 885 (2019)
126. J. Shi, Y. Huan, X. Zhao, P. Yang, M. Hong, C. Xie, S. Pennycook, and Y. Zhang, Two-dimensional metallic vanadium ditelluride as a high-performance electrode material, *ACS Nano* 15(1), 1858 (2021)
127. Z. Zhou, F. Yang, S. Wang, L. Wang, X. Wang, C. Wang, Y. Xie, and Q. Liu, Emerging of two-dimensional materials in novel memristor, *Front. Phys.* 17(2), 23204 (2022)
128. L. Du, Z. Wang, and G. Zhao, Novel intelligent devices: Two-dimensional materials based memristors, *Front. Phys.* 17(2), 23602 (2022)
129. H. Yu, A. Kutana, and B. I. Yakobson, Carrier delocalization in two-dimensional coplanar p–n junctions of graphene and metal dichalcogenides, *Nano Lett.* 16(8), 5032 (2016)
130. Y. Zhang, L. Yin, J. Chu, T. A. Shifa, J. Xia, F. Wang, Y. Wen, X. Zhan, Z. Wang, and J. He, Edge-epitaxial growth of 2D NbS_2-WS_2 lateral metal–semiconductor heterostructures, *Adv. Mater.* 30(40), 1803665 (2018)
131. Q. Fu, X. Wang, J. Zhou, J. Xia, Q. Zeng, D. Lv, C. Zhu, X. Wang, Y. Shen, X. Li, Y. Hua, F. Liu, Z. Shen, C. Jin, and Z. Liu, One-step synthesis of metal/semiconductor heterostructure NbS_2/MoS_2, *Chem. Mater.* 30(12), 4001 (2018)
132. X. Wang, Z. Wang, J. Zhang, X. Wang, Z. Zhang, J. Wang, Z. Zhu, Z. Li, Y. Liu, X. Hu, J. Qiu, G. Hu, B. Chen, N. Wang, Q. He, J. Chen, J. Yan, W. Zhang, T. Hasan, S. Li, H. Li, H. Zhang, Q. Wang, X. Huang, and W. Huang, Realization of vertical metal semiconductor heterostructures via solution phase epitaxy, *Nat. Commun.* 9(1), 3611 (2018)
133. X. Zhai, X. Xu, J. Peng, F. Jing, Q. Zhang, H. Liu, and Z. Hu, Enhanced optoelectronic performance of CVD-grown metal–semiconductor $NiTe_2/MoS_2$ heterostructures, *ACS Appl. Mater. Interfaces* 12(21), 24093 (2020)
134. W. S. Leong, Q. Ji, N. Mao, Y. Han, H. Wang, A. J. Goodman, A. Vignon, C. Su, Y. Guo, P. C. Shen, Z. Gao, D. A. Muller, W. A. Tisdale, and J. Kong, Synthetic lateral metal–semiconductor heterostructures of transition metal disulfides, *J. Am. Chem. Soc.* 140(39), 12354 (2018)
135. J. Li, X. Yang, Y. Liu, B. Huang, R. Wu, Z. Zhang, B. Zhao, H. Ma, W. Dang, Z. Wei, K. Wang, Z. Lin, X. Yan, M. Sun, B. Li, X. Pan, J. Luo, G. Zhang, Y. Liu, Y. Huang, X. Duan, and X. Duan, General synthesis of two-dimensional van der Waals heterostructure arrays, *Nature* 579(7799), 368 (2020)